JOURNAL OF THE ROYAL SOCIETY Interface

J. R. Soc. Interface (2010) **7**, 1205–1218
doi:10.1098/rsif.2010.0032
Published online 24 March 2010

Cerebrospinal fluid dynamics in the human cranial subarachnoid space: an overlooked mediator of cerebral disease. II. *In vitro* arachnoid outflow model

David W. Holman[1,2], Vartan Kurtcuoglu[3] and Deborah M. Grzybowski[1,2,*]

[1]*Biomedical Engineering Department, and* [2]*Ophthalmology Research Division, Ohio State University, 915 Olentangy River Road, Columbus, OH 43212, USA*
[3]*Laboratory of Thermodynamics in Emerging Technologies, Department of Mechanical and Process Engineering, ETH Zurich, Zurich, Switzerland*

The arachnoid membrane (AM) and granulations (AGs) are important in cerebrospinal fluid (CSF) homeostasis, regulating intracranial pressure in health and disease. We offer a functional perspective of the human AM's transport mechanism to clarify the role of AM in the movement of CSF and metabolites. Using cultures of human AG cells and a specialized perfusion system, we have shown that this *in vitro* model mimics the *in vivo* characteristics of unidirectional fluid transport and we present the first report of serum-free permeability values (92.5 $\mu l\ min^{-1}\ mm\ Hg^{-1}\ cm^{-2}$), which in turn are in agreement with the CSF outflow rates derived from a dynamic, *in vivo* magnetic resonance imaging-based computational model of the subarachnoid cranial space (130.9 $\mu l\ min^{-1}\ mm\ Hg^{-1}\ cm^{-2}$). Lucifer yellow permeability experiments have verified the maintenance of tight junctions by the arachnoidal cells with a peak occurring around 21 days post-seeding, which is when all perfusion experiments were conducted. Addition of ruthenium red to the perfusate, and subsequent analysis of its distribution post-perfusion, has verified the passage of perfusate via both paracellular and transcellular mechanisms with intracellular vacuoles of approximately 1 μm in diameter being the predominant transport mechanism. The comparison of the computational and *in vitro* models is the first report to measure human CSF dynamics functionally and structurally, enabling the development of innovative approaches to modify CSF outflow and will change concepts and management of neurodegenerative diseases resulting from CSF stagnation.

Keywords: cerebrospinal fluid; intracranial pressure regulation; arachnoid; Alzheimer's disease; hydrocephalus; *in vitro* model

1. INTRODUCTION

While cerebrospinal fluid (CSF) may have once been regarded as simply a fluid cushion for the brain, the CSF also offers nutritive and signalling functions to the cells of the brain and its membranes (the central nervous system, CNS), and fluid pressure control functions to maintain homeostasis.

Disorders of the CNS such as Alzheimer's disease, subarachnoid haemorrhage, pseudotumour cerebri and hydrocephalus include loss of CSF pressure regulation (Segal 2000; Stopa 2001; Abbott 2005; Johanson *et al.* 2005). Many of the recognizable signs of brain disease are changes that reflect disrupted CSF homeostasis and the resultant damage from the build-up of pressure and toxic metabolites. The mechanism for a multitude of pathological conditions including subarachnoid haemorrhage, pseudotumour cerebri, hydrocephalus and Alzheimer's disease is believed to be an increased resistance to the outflow of CSF or a totally decreased CSF flow (Martins *et al.* 1974; Jones 1985; Johnston *et al.* 1991; Johnston & Teo 2000; Levine 2000; Johanson 2001, 2004; Johanson *et al.* 2005). A major portion of CSF outflow is believed to occur through the arachnoid membranes (AMs) including the granulations (AGs) and villi with a contribution through the extra-cranial lymphatics as well. In addition, there is a new and important concept of CSF retention or stagnation, with the formation of a 'ventricular sink' of metabolic products of neurodegeneration, and their role as neurotoxins in the cascade of events leading to the signs and symptoms of diseases such as Alzheimer's disease, and to their progression (Stopa 2001; Kivisakk 2003; Silverberg *et al.* 2003).

*Author for correspondence (deborah.grzybowski@osumc.edu).

Received 25 January 2010
Accepted 1 March 2010

Further research is necessary to increase our understanding of CSF outflow regulated by the AM and the role of AM in pathological conditions. It has been suggested that a more refined functional and structural pathology of the AM is needed on the absorptive mechanism to understand the role AM plays in the clearance of CSF and toxic metabolites (Johnston & Teo 2000).

In order to understand the role of arachnoid cells in the CSF outflow and its pathologies, we have developed a human *in vitro* cell culture model. We have previously grown and characterized cells from human AG tissue in terms of their morphology and expression of proteins (Holman *et al.* 2005). We have also demonstrated that human AG cells *in vitro* display a preferential unidirectionality of fluid flow that is in agreement with the physiological flow of CSF in the body (Grzybowski *et al.* 2006). In this present study, we expand on these preliminary efforts and further characterize the serum-free permeability characteristics of cultured human AG cells and compare these data to a dynamic, *in vivo* magnetic resonance imaging (MRI)-based computational model of CSF movement through the subarachnoid cranial space (Gupta *et al.* 2010).

Further characterization of this model will affect our concepts and management of neurodegenerative diseases resulting from CSF stagnation. The near-term goal is to find novel ways to modulate CSF outflow and content; long-term application is to control disorders that accumulate toxic metabolites in CSF and which disrupt normal barrier functions in the CNS. Modification of CSF outflow to retain and prolong the action of therapeutic agents in diseases such as metastatic brain cancer, meningitis and multiple sclerosis (MS) will offer treatment benefits not currently possible.

2. MATERIAL AND METHODS

2.1. AG cell culture and characterization

AG cells were grown and characterized using the methods described by Holman *et al.* (2005). Briefly, brain tissue was obtained within 24 h post-mortem from the Ohio State University Regional Autopsy Center. Collection was in accordance with guidelines and regulations set forth by the Office of Responsible Research Practices Institutional Review Board for human subjects at the Ohio State University. The tissues used for these experiments were from cases without gross neurological involvement (no Alzheimer's disease, brain tumours, MS, subarachnoid haemorrhage, etc.). Tissues collected from 17 donors, of an average age of 60, were used. At autopsy, AGs were collected from the superior sagittal sinus and adjacent lateral lacunae tissue. Using a dissecting microscope, individual granulations were excised and explanted into wells of a fibronectin-coated culture plate. When confluent, cells were passaged and plated to fibronectin-coated T-25 cm^2 culture flasks. Each donor was passaged independently to a maximum of four passages.

2.2. AG cell media formulations

Primary cultures from AG explants and AG cells grown in subsequent passages were grown in media containing 10 per cent serum as described previously (Holman *et al.* 2005).

2.3. Immunocytochemical characterization of human AG cells

AG cells were characterized in culture as described previously (Holman *et al.* 2005). Briefly, second or third passage cells were seeded onto 22 mm fibronectin-coated coverslips (Becton Dickinson, Franklin Lakes, NJ, USA) and grown to confluency. Cell cultures were tested at 1–1.5 weeks post-confluency for the presence of cytokeratins (1 : 50, Dako Cytomation, Carpinteria, CA, USA), vimentin (1 : 100, Sigma–Aldrich, St Louis, MO, USA), desmoplakin 1 and 2 (1 : 40, Chemicon International, Temecula, CA, USA), occludin and ZO-1 (both 1 : 50 Zymed, San Francisco, CA, USA) protein expression.

The cells were washed three times with sterile Dulbecco's phosphate-buffered saline (D-PBS) and fixed with 3.7 per cent paraformaldehyde for 10 min, then permeabilized with 0.2 per cent Triton X-100 (Sigma–Aldrich, St Louis, MO, USA) in phosphate-buffered saline (PBS) at 37°C for 5 min. Coverslips were incubated for 30 min in 10 per cent calf serum in D-PBS to block non-specific binding of the primary antibody, and then incubated with the primary antibodies for 45 min at 37°C. Secondary antibodies were an Alexa Fluor 555 conjugated donkey anti-mouse IgG1 (for desmoplakin and cytokeratin) and an Alexa Fluor 555 conjugated goat anti-rabbit IgG1 antibody (for occludin). ZO-1 expression was detected by a fluorescein isothiocyanate (FITC)-conjugated mouse anti-ZO-1 antibody. Vimentin expression was detected by a Cy-3-conjugated mouse anti-vimentin antibody.

Cells were then washed in D-PBS and incubated with the secondary antibody for 45 min, washed again in D-PBS, counterstained with 4′,6-diamidino-2-phenylindole (DAPI) and mounted with an antifade reagent (Prolong Gold with DAPI, Molecular Probes) onto slides for visualization. The cell cultures were visualized using a Zeiss Axiocam inverted microscope equipped with DAPI, FITC and Cy3 filter sets.

2.4. Seeding AG cells to cell culture inserts

For functional characterization of AG cells, second or third passage cultures were seeded to permeable cell culture inserts (Millipore, Billerica, MA, USA). Cell culture insert specifications were 12 mm diameter track-etched polycarbonate with a 0.4 μm pore size and a 0.6 cm^2 effective growth area. Cells were seeded to inserts at a density of 5.0×10^5 cells cm^{-2} (3×10^5 cells per insert) based on the manufacturer's specifications. Cell growth on the inserts before perfusion was monitored with time by measuring the lucifer yellow (LY) permeability.

2.5. Lucifier yellow permeability assay

After seeding AG cells to culture inserts, barrier integrity of each insert was monitored with time by measuring LY permeability. A stock LY solution was made by dissolving LY (LY dipostassium salt, Sigma Aldrich) in basal media (DMEM/F12 50 : 50 v/v) to a

concentration of 4 mM. The stock solution was diluted to a working solution of 200 μM. Media was removed from inside the insert (apical side), and replaced with a 100 μM solution of LY in basal media. Cell culture media was also removed from the well surrounding the insert (basolateral side), and replaced with basal media. The height of the fluid in the apical and basolateral chambers was the same to eliminate any hydrostatic pressure effects. To determine the permeability characteristics of the culture insert alone, a blank insert without cells was tested in the same manner.

Inserts were incubated for 2 h at 37°C on a plate shaker to ensure a well-mixed uniform concentration of LY on each side of the insert. After incubation, 4 × 100 μl aliquots were sampled from the basolateral side of each culture insert. Samples were analysed using a CytoFluor 4000 fluorescence multi-well plate reader (Applied Biosystems, Foster City, CA, USA), with 485 nm excitation wavelength and 530 nm emission. To correlate the measured fluorescent units to concentration values, a standard curve was prepared from a series of dilutions of LY in basal media. The intrinsic fluorescence of basal media was measured and subtracted from all fluorescence values. The permeability of the cell layer is reported as a permeability coefficient, P_{cells} (in cm s^{-1}). For a detailed description of the calculation of the permeability coefficient, P_{cells}, see the review by Deli *et al.* (2005).

2.6. Perfusion system

AG cells were characterized in a specialized perfusion chamber as described by Grzybowski *et al.* (2006). Briefly, the cell perfusion system consisted of a modified Ussing chamber, connected through tubing to a fluid reservoir that provided the hydrostatic pressure gradient. To maintain cell viability, the perfusion system was placed in an incubator at 37°C.

The pressure drop across the cell layer was continuously monitored by an in-line pressure transducer interfaced with a data acquisition computer. A second pressure transducer monitored atmospheric pressure during perfusion. We determined average volumetric flow rate by collecting and measuring the volume of perfusate over the duration of the perfusion. The perfusate collection port was kept at the same height as that of the filter insert to ensure that the pressure drop measured at the cell layer represented the actual pressure drop across the cell layer.

Cells were perfused for 4 h in the physiological direction, mimicking normal CSF flow *in vivo* from the subarachnoid space across the AGs to the venous sinuses. For cells perfused in the physiological direction, the fluid first flowed through the filter membrane, then the basolateral side of the cell layer and finally through the apical cell membrane. This is hereafter referred to as the basolateral to apical (B → A) direction. Cells were also perfused for 4 h under similar conditions in the opposite, non-physiological direction simulating the condition of an increase in the venous sinus pressure above the CSF pressure. For cells perfused in the non-physiological apical to basolateral (A → B) direction, the fluid first passed through the apical cell membrane, then the basolateral membrane, and finally the filter membrane.

2.7. Calculation of cellular hydraulic conductivity

The cellular hydraulic conductivity ($L_{\text{p,cells}}$) depends on the surface area of the confluent cell layer on the insert, the volumetric flow rate and the pressure drop across the cell layer. The cellular hydraulic conductivity was calculated according to the following equation:

$$L_{\text{p,cells}} = \frac{Q_{\text{cells + filter}}}{\Delta P A (1 - (Q_{\text{cells + filter}} / Q_{\text{filter}}))}.$$

From this equation, the cellular hydraulic conductivity, $L_{\text{p,cells}}$, can be calculated since the surface area of the confluent cell layer, A, is known and assumed to be equal to the filter; the transcellular pressure drop, ΔP, can be calculated based on the pressure across the cell layer plus filter, and atmospheric pressure ($\Delta P_{\text{transcellular}} = P_{\text{cell layer+filter}} - P_{\text{atmospheric}}$); the flow rate across the cells and filter, $Q_{\text{cells+filter}}$, is calculated; and the flow rate across the filter, Q_{filter}, is measured experimentally by perfusing empty filters without cells and calculating the average volumetric flow rate and L_{p} across the filter alone.

A detailed derivation of the formula used to calculate the cellular hydraulic conductivity is given by Grzybowski *et al.* (2006). To determine the hydraulic conductivity of the culture insert alone, blank culture inserts without cells were perfused in an identical manner.

2.8. Post-perfusion analysis

After perfusion, AG cells on inserts were examined in several ways. The effect of perfusion on cellular viability was determined using a commercially available cytotoxicity assay. The effects of perfusion under pressure on AG cell expression of the tight junction protein ZO-1 was examined using laser scanning confocal microscopy. Cellular ultrastructure was examined with electron microscopy (EM) and, in some cases, the tracer ruthenium red was used to highlight the path of fluid flow and delineate cellular membranes.

2.9. Viability assay

Cell viability was assessed by a live–dead viability/cytotoxicity kit (Molecular Probes). Cells were incubated with a solution of 2 μM calcein AM and 4 μM ethidium homodimer-1 in PBS for 40 min at 37°C. Cells showing diffuse cytoplasmic green fluorescence indicated live cells with ubiquitous intracellular esterase activity, while dead or dying cells were designated by localized nuclear red fluorescence resulting from damaged membrane integrity.

The percentage of dead cells was calculated by counting the number of red nuclei in five microscope fields. The average number of dead cells per field was used to determine the percentage of dead cells using the area of the microscope field and the confluent density of AG cells grown on a culture insert (approx. 3.3×10^5 cells cm^{-2}).

2.10. Laser scanning confocal microscopy

After perfusion, cells were analysed for the presence of tight junctions using laser scanning confocal microscopy. Following perfusion, the culture media was flushed from the upstream perfusion chamber and 3.7 per cent paraformaldehyde was infused into the upstream chamber using a 20 cm^3 syringe at the same pressure as perfusion. Cells on filters were fixed under pressure for 20 min, removed from the perfusion chamber and post-fixed for an additional 15 min. Cells were perfused and fixed under the same pressure gradient, both magnitude and direction. After fixation, the inserts were labelled with a FITC-conjugated anti-ZO-1 antibody as described above and counter-stained with a DRAQ5 nuclear stain (Biostatus Limited, Leicestershire, UK) for 5 min at a 1 : 500 dilution, excised from their casing, mounted onto a microscope slide, sealed and coverslipped. As a control, non-perfused AG cells grown on inserts were stained in an identical manner. Slides were visualized using a Zeiss 510META laser scanning confocal microscope equipped with red helium-neon, green helium-neon and argon lasers. Confocal images were acquired at 1024×1024 resolution and Z-stack images were acquired by capturing approximately 1 μm thick optical slice images in the z-plane through the thickness of the cell layer.

2.11. Electron microscopy

AG cells were perfused and fixed under pressure and cellular ultrastructure was examined by EM. Following perfusion, the culture media was flushed from the upstream perfusion chamber and a 3 per cent glutaraldehyde solution in 0.1 M phosphate buffer with 0.1 M sucrose was infused into the upstream chamber using a 20 cm^3 syringe and cells were fixed at the same pressure as perfusion. Cells on filters were fixed under pressure for 45 min, and then removed from the perfusion chamber and fixed for an additional 30 min. Cells were perfused and fixed under the same pressure gradient, both magnitude and direction. As a control, AG cells grown on inserts that were not perfused were fixed and processed in an identical manner. For ruthenium red tracer studies, ruthenium red was dissolved in the glutaraldehyde and osmium tetroxide fixatives to a final concentration of 0.1 per cent. In ruthenium red tracer experiments, the fixative was dissolved in cacodylate buffer as ruthenium red precipitates in phosphate buffers.

Cells were post-fixed in 1 per cent osmium tetroxide in 0.1 M phosphate (or cacodylate for ruthenium red tracer experiments) buffer containing 0.1 M sucrose, pH 7.4 for 1 h. They were then rinsed, stained (2% uranyl acetate for 30 min) and dehydrated via graded ethanols. Samples were incubated in two varying concentrations of hydroxypropyl methacrylate and rinsed five times in 100 per cent Polybed 816, then embedded in Polybed 812 in a round silicon mould and polymerized at 60°C for 24 h. Embedded samples were sectioned on a Leica EM UC6 ultramicrotome at 70 nm. Sections were picked up on 100 mesh formvar-coated grids stained with 2 per cent uranyl acetate and Reynolds lead citrate and finally examined under a Phillips CM12 transmission electron microscope (TEM) at 80 kV.

2.12. Data analysis

Data presented are representative of at least three or more experiments of AG cells grown from three separate tissue donors to ensure reproducibility. Data are expressed as mean ± s.e. Treatment effects were evaluated using a two-sided Student's t-test unless indicated otherwise, and $p < 0.05$ was taken as statistically significant.

3. RESULTS

3.1. AG cell growth and characterization

AG cells in culture grew in monolayers, exhibited a polygonal morphology and were packed densely to form a cobblestone-like appearance characteristic of epithelial cell types (figure 1*a*). Cultures of AG cells expressed the desmosomal junctional proteins desmoplakin 1 and 2 at cell borders (figure 1*b*), where desmosomes mediate cell–cell attachments. Finally, human AG cells were immunoreactive to the anti-ZO-1 and anti-occludin antibodies indicating that AG cells expressed tight junction proteins (figure 1*c*,*d*, respectively). AG cells also expressed the intermediate filament proteins cytokeratin and vimentin (figure 1*e*,*f*, respectively). The expression of these markers was used as confirmation that the cells cultured and used for experiments were arachnoidal in origin.

3.2. Lucifier yellow permeability results

As a functional means of assessing tight junction formation, cells were monitored with time for their permeability to the hydrophilic macromolecule LY. The paracellular flux of LY across AG cell layers was determined by measuring the permeability coefficient (P_{cells} in cm s^{-1}) of LY across AG cells seeded on permeable cell culture inserts.

The results of the LY permeability test on AG cells are summarized in figure 2 and below for the weekly time points. LY permeability coefficients for AG cells on inserts were $11.04 \pm 1.82 \times 10^{-6}$ cm s^{-1} on day 7, $12.67 \pm 1.90 \times 10^{-6}$ cm s^{-1} on day 14, $7.19 \pm 0.82 \times 10^{-6}$ cm s^{-1} on day 21, $10.77 \pm 0.94 \times 10^{-6}$ cm s^{-1} on day 28 and $14.65 \pm 1.35 \times 10^{-6}$ cm s^{-1} on day 35 post-seeding. There was a statistically significant decrease in LY permeability at day 21 compared with days 14 and 28 (p-values of 0.02 and 0.01, respectively), indicating that the barrier integrity of the AG cell layer was greatest at 21 days post-seeding. Based on these results, AG cells on inserts were perfused approximately 21 days after seeding. This ensured that the flow rates measured in the perfusion studies were because of flow across an intact cell layer with fully developed cell–cell junctions.

3.3. Serum-free media viability

The effect of serum on the hydraulic conductivity was confirmed by perfusing blank inserts using media with and

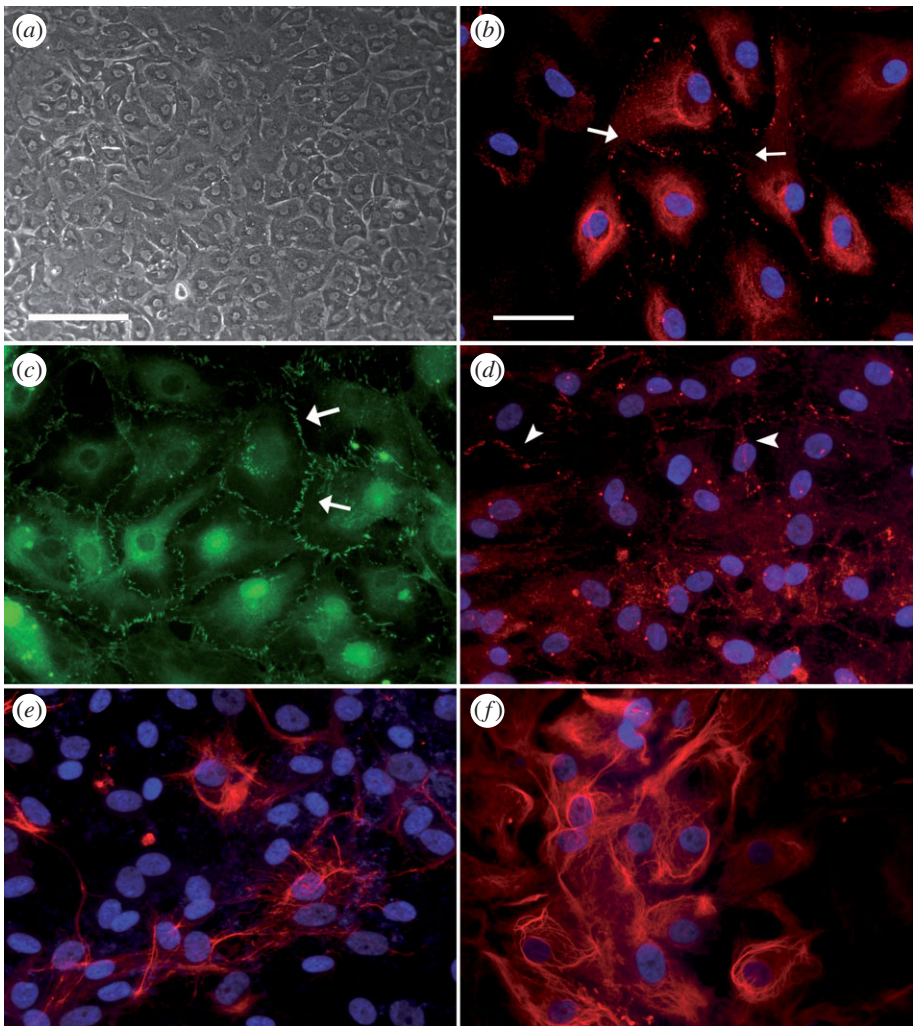

Figure 1. Culture and characterization of cells grown from human AG tissue. Primary cultures of AG cells at passage number 2 and 3 were stained with antibodies to several junctional and cytoskeletal proteins and visualized with fluorescently conjugated secondary antibodies. Fluorescently conjugated antibodies were either AlexaFluor488 (green) or AlexaFluor555 (red). Cultures were counterstained with DAPI (blue) to label cell nuclei and visualized using an inverted fluorescent microscope. (*a*) AG cells in culture grew as cuboidal cells that packed-in densely in culture to form a monolayer. (*b*) AG cells expressed the protein desmoplakin, positive staining is between adjacent cell–cell membranes (white arrows). (*c*) AG cells expressed the tight junction protein ZO-1 between cells as short finger-like projections (white arrows). (*d*) AG cells expressed the tight junction protein occludin at cell borders (white arrowheads). (*e*) Cytokeratin and (*f*) vimentin immunoreactivity was demonstrated by labelling with a broad spectrum cytokeratin antibody or a monoclonal antibody to vimentin. Scale bars, (*a*) 200 μm; (*b–f*) 50 μm.

without serum. Results of these studies are shown in table 1. The average hydraulic conductivity of blank culture inserts perfused with serum-free media (SFM; $n = 6$ inserts) was 328.79 ± 23.12 μl min^{-1} mm Hg^{-1} cm^{-2} with an average pressure drop across the culture insert of 3.38 ± 0.23 mm Hg. The average hydraulic conductivity of blank culture inserts perfused with media plus 10 per cent serum ($n = 6$ inserts) was 5.58 ± 0.91 μl min^{-1} mm Hg^{-1} cm^{-2} with an average pressure drop across the culture insert of 3.17 ± 0.092 mm Hg. There is a statistically significant difference in hydraulic conductivity between the two groups ($p < 0.0001$) despite being perfused under similar pressures ($p = 0.40$). Further perfusion experiments were carried out using SFM to characterize the hydraulic conductivity of AG cells without the effect of serum.

In order to demonstrate that AG cells could remain viable in SFM, cells were first grown to confluence on coverslips in media with serum. Three coverslips were incubated in SFM. One coverslip remained in media supplemented with 10 per cent serum as a control (time point = 0 h). At time points 4, 8 and 12 h, a coverslip was washed, and labelled using the live–dead viability and cytotoxicity assay. The time point 0 s served as the control and the viability of the cells at each subsequent time point was expressed as a fold increase in dead cells relative to time = 0 h. There was not a statistically significant increase in the number of dead cells at any time point when compared with the control at 0 h ($n = 4$ for each time point). In general, the viability of AG cells maintained in SFM was between 97 and 98 per cent (approx. 2–3% dead cells) and was never less than 95 per cent viable at any time point.

Next, cells were seeded to culture inserts and perfused in SFM for 4 h in the physiological B → A direction. As a control, two inserts with cells were not perfused; one was kept in media plus 10 per cent

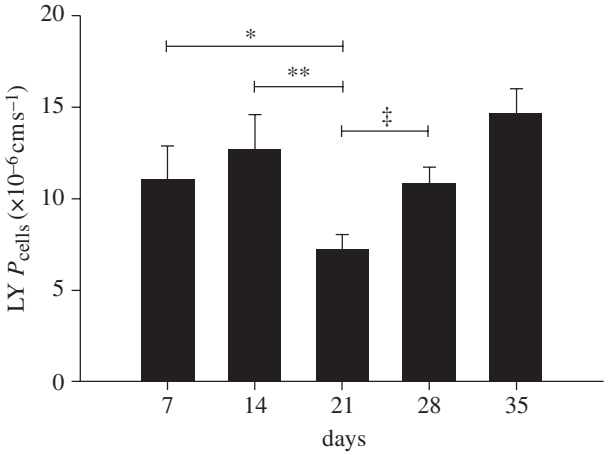

Figure 2. Summary of AG cell LY permeability with time. AG cells grown on permeable cell culture inserts were tested at various time points for their permeability to the hydrophilic macromolecule LY. The average LY permeability coefficient (P_{cells} expressed as $\times 10^{-6}$ cm s^{-1}) for the weekly time points $\pm$s.e. is shown against time. There was no statistical difference between LY permeability on day 7 ($n = 34$ inserts) and day 14 ($n = 34$ inserts). LY permeability decreased significantly from day 14 to day 21 ($n = 30$ inserts). After 21 days, LY permeability increased at both 28 ($n = 18$ inserts) and 35 days ($n = 9$ inserts) post-seeding. These results indicate that LY permeability and therefore barrier integrity was greatest approximately 21 days after seeding. $^{*}p < 0.07$; $^{**}p < 0.02$; $^{‡}p < 0.01$.

serum and the other in SFM. After 4 h, inserts were removed from the perfusion system and labelled with the viability assay. SFM-perfused cells ($n = 8$ inserts) showed an increase in the number of dead cells compared with the non-perfused SFM ($n = 3$ inserts) and media plus serum ($n = 3$ inserts) controls; however the increase was not statistically significant. AG cells perfused in SFM had a viability of 97.22 ± 0.51 per cent compared with non-perfused media plus serum and SFM controls that had viabilities of 97.70 ± 1.03 and 98.05 ± 0.69 per cent, respectively. These results indicate that perfusion under pressure does not significantly affect the viability of AG cells compared with non-perfused controls and confirm that AG cell viability is maintained during perfusion in SFM.

3.4. Serum-free media perfusion results

In SFM, the hydraulic conductivity of blank culture inserts (no cells) was 328.79 ± 23.12 µl min^{-1} mm Hg^{-1} cm^{-2} ($n = 6$) and was significantly greater than the cellular hydraulic conductivity (cells only) of AG cells perfused in SFM, which was 92.49 ± 11.79 µl min^{-1} mm Hg^{-1} cm^{-2} ($n = 17$; $p < 0.0001$) when perfused at the same pressure after eliminating the filter resistance as previously published (Grzybowski *et al.* 2006). These results indicate that in SFM, the resistance of the culture insert is significantly less than the resistance of the AG cell layer and likely did not affect the measurement of the true cellular hydraulic conductivity.

Table 2 provides a summary of AG cell perfusions in SFM in both the physiological (B → A) and non-physiological (A → B) directions. There was a statistically significant difference in the average cellular hydraulic conductivity between the physiological B → A and non-physiological A → B perfusion ($p < 0.001$) directions, despite being perfused under similar pressures ($p = 0.07$).

In order to characterize the pressure–flow rate response of this *in vitro* model, AG cells were grown on culture inserts and perfused over a range of pressures. Cells were perfused starting at a 2 mm Hg pressure drop for 2 h during which time perfusate was collected and the flow rate was measured. Next, the pressure was raised at 2 mm Hg intervals and the perfusate collected over a period of 2 h for pressure drops of 4, 6 and 8 mm Hg. Each time when the pressure was increased, the system was allowed to equilibrate for 30 min at the new level before pressure data were recorded and perfusate collected. The results of this experiment are shown in figure 3 and the data represent a total of four inserts from two separate tissue donors at each pressure. Linear regression analysis of this data gives a slope of 0.0295 ml min^{-1} mm Hg^{-1} and an R^2 value of 0.9948.

At the conclusion of these experiments, cells on inserts were removed from the perfusion chamber and stained with the live–dead viability assay as described above. Viability assessment of perfused cells indicated that cells remained viable and attached to the culture insert (results not shown). Cells were not perfused at higher pressures, as a pilot experiment indicated that at pressures greater than 8 mm Hg, the cell layer became disrupted, particularly at the centre of the insert near the upstream inlet port.

3.5. Laser scanning confocal microscopy post-perfusion analysis

To examine whether AG cells maintained tight junctions after being perfused under pressure, cells on inserts were perfused and fixed under physiological ($n = 3$ inserts) and non-physiological ($n = 2$ inserts) conditions, labelled with a FITC-conjugated anti-ZO-1 antibody, counterstained with a DRAQ5 nuclear stain and visualized using a laser scanning confocal microscope. As a control, AG cells were seeded to inserts but not perfused ($n = 2$ inserts), and were subsequently labelled with the anti-ZO-1-FITC antibody and visualized on the confocal microscope.

Z-stack images were taken for each sample with approximately 1 µm optical slices to provide en face images of the X–Z and Y–Z planes. These Z-stack images (figure 4) provide an additional cross-sectional view of the cell layer and confirm that ZO-1 expression is limited to cell–cell borders.

AG cells on inserts that were not perfused (figure 4*a*, ×100 magnification), perfused non-physiologically A → B (figure 4*b*, ×40 magnification), or perfused physiologically B → A (figure 4*c*, ×63 magnification) showed similar patterns of expression of the ZO-1 protein, localized in a characteristic pattern at cell–cell borders. The expression of the ZO-1 protein at cell borders was similar to that described in Schlemm's canal endothelial cells, with a discontinuous palisading pattern of ZO-1 protein at short filapodia extending between adjacent cell membranes (Alvarado *et al.* 2004).

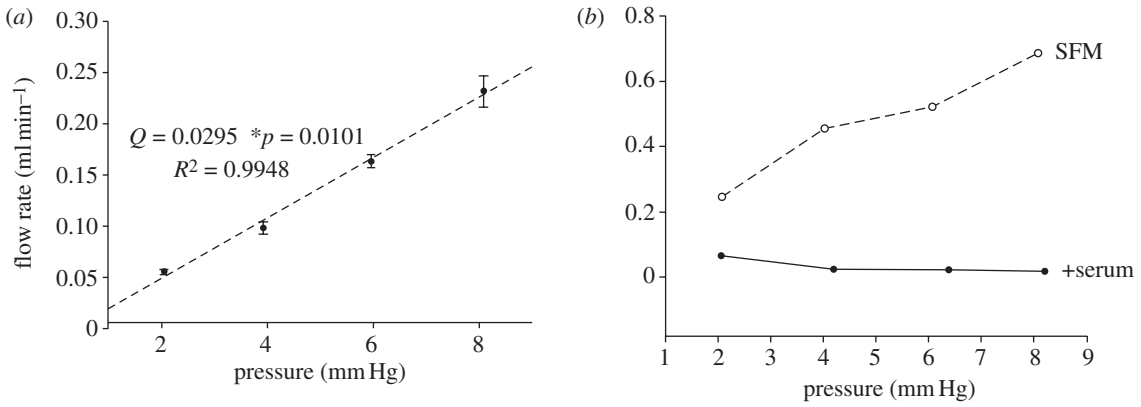

Figure 3. Pressure–flow rate experimental relationship. Flow rates were obtained experimentally over a range of pressures (2–8 mm Hg). (*a*) AG cells on inserts in SFM. Each data point represents four inserts from two donors. (*b*) Blank inserts were perfused under the same pressures as the AG cells in (*a*) using both SFM and media with 10 per cent serum. These results indicate that the relationship between pressure and CSF outflow is linear over the range tested. In addition, under serum-free conditions, the filter is not the rate-limiting factor.

Table 1. Perfusion results for blank culture inserts perfused B → A in media with and without serum.

	media + 10% serum ($n = 6$)	serum-free media ($n = 6$)	p-value
ave P (mm Hg)	3.17 ± 0.092	3.38 ± 0.23	0.40
ave L_p (μl min^{-1} mm Hg^{-1} cm^{-2})	5.58 ± 0.91	328.79 ± 23.12	<0.0001

Table 2. Perfusion results for AG cells only using serum-free media.

	A → B ($n = 6$)	B → A ($n = 17$)	p-value
ave P (mm Hg)	3.24 ± 0.16	2.91 ± 0.085	0.069
ave L_p (μl min^{-1} mm Hg^{-1} cm^{-2})	0.00 ± 0.00	92.49 ± 11.79	0.0002

It appears that the AG cell expression of the tight junction protein ZO-1 is unchanged by the perfusion conditions. Taken together, these results suggest that ZO-1 expression is localized to cell–cell contacts and that barrier integrity remains intact while the cell layer is under pressure, regardless of perfusion direction or presence of serum.

3.6. EM post-perfusion analysis

Transmission EM was used to examine the cellular ultrastructure of AG cells perfused and fixed under 3 mm Hg pressure in the physiological (B → A, $n = 3$ inserts) and non-physiological (A → B, $n = 1$ insert) directions. In addition, as a control ($n = 2$ inserts), cells on inserts that were not perfused were fixed and processed in an identical manner.

The ultrastructure of non-perfused control cells and cells perfused and fixed in the A → B direction (figure 5) appeared similar to those described previously for AG cells perfused with serum, indicating that the serum-free conditions did not alter this cellular function (Grzybowski *et al.* 2006). The cell layer remained closely apposed to the filter membrane and there were few spaces between overlapping cellular processes.

Figure 5*a* shows AG cells perfused with SFM and fixed under pressure. The large open arrow indicates the direction of fluid flow, with several cell nuclei (N) visible. Structures (filled stars), similar to vacuoles in size (1 μm) and shape, described in cultured Schlemm's canal endothelial cells (Alvarado *et al.* 2004) are apparent projecting from the apical edge of the cell layer. These structures also appear similar to vacuoles projecting into the dural venous sinuses described in intact AG tissue. Two additional regions of interest are boxed and examined more closely in figure 5*b*,*c*.

These micrographs indicate it is possible that cultured AG cells fixed under pressure can form intracellular vacuoles that resemble those seen in the Schlemm's canal endothelial cells as well as arachnoidal cells lining the AG tissue.

3.7. EM analysis with ruthenium red tracer

AG cells on inserts were also perfused and fixed under pressure using glutaraldehyde with the tracer ruthenium red dissolved in the fixative to a final concentration of 0.1 per cent. Inserts were perfused and fixed in the A → B ($n = 3$ inserts) or B → A ($n = 3$ inserts) directions and examined via TEM. The tracer is visible in the micrographs as dark, electron-dense material accentuating cell membranes and processes.

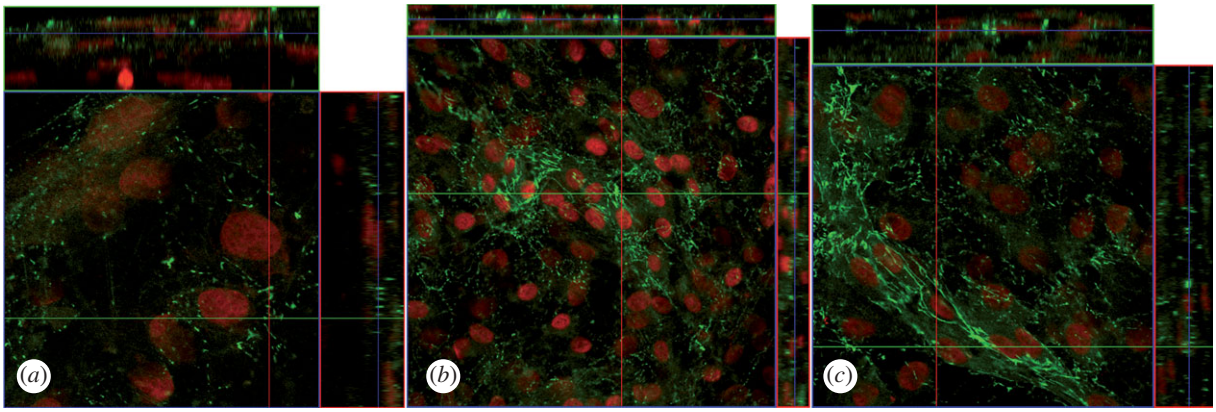

Figure 4. Laser scanning confocal microscopy analysis of ZO-1 protein expression in perfused AG cells. AG cells were seeded to culture inserts, perfused under pressure and labelled with an FITC-conjugated anti-ZO-1 antibody (green) to examine the expression of tight junctions in perfused AG cells. Cells on inserts were counterstained with DRAQ5 to label nuclei (red). Z-stack images were acquired by taking 1 μm optical sections through the entire cell layer in order to visualize cell–cell borders that were not entirely visible in a single focal plane. (*a*) As a control, cells were grown on inserts but were not perfused, ×100 magnification. (*b*) AG cells perfused in the non-physiological A → B direction, ×40 magnification. (*c*) AG cells perfused in the physiological B → A direction, ×63 magnification.

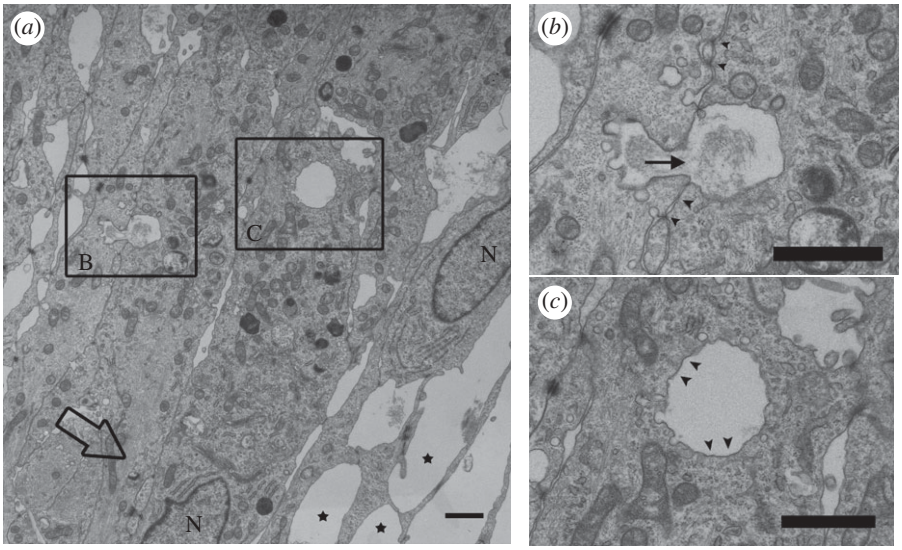

Figure 5. TEM analysis of AG cells fixed under B → A pressure. AG cells were perfused and fixed under B → A pressure (large open arrow). (*a*) Protrusions of the apical cell membrane (filled stars) appear similar to vacuoles projecting into the dural venous sinuses described in intact AG tissue. Several cell nuclei (N) are also visible near the apical edge of the cell layer. (*b*) A vacuole is visible fusing at the apical edge of one cell and beginning to invaginate at the basolateral cell membrane of an adjacent overlapping cell. Electron-dense material on either side of this structure (filled arrowheads) may represent cell–cell junction between overlapping cells. (*c*) An intracellular vacuole with an intact membrane lining (filled arrowheads) appears to be completely contained within the cell cytoplasm. The filled arrow specifies the direction of fluid flow. Scale bars, 1 μm.

For ruthenium red tracer experiments, two different non-perfused controls were prepared to compare with the two different perfusion directions. Apical controls ($n = 2$ inserts) received fixative plus 0.1 per cent ruthenium red inside the insert to expose the apical aspect of the cell layer to the tracer, while the well surrounding the insert received fixative without tracer. Similarly, basolateral controls ($n = 2$ inserts) received fixative alone inside the insert, while the well surrounding the inserts contained fixative plus ruthenium red to expose the basolateral side of the cell's layer to the tracer.

Apical control cells and cells perfused and fixed under A → B pressure with fixative plus ruthenium red are shown in figure 6. The filter membrane is indicated but not shown, as it was somewhat disintegrated during processing and embedding.

An area of interest is boxed and examined in greater detail in figure 6*b*. The expanded view shown in figure 6*b* illustrates an area where the penetration of the tracer is impeded and does not infiltrate further into the cell layer. While there are no cellular junctions visible at this point in this particular section, it is likely that occluding junctions are preventing further penetration of the tracer.

The area of greater detail in figure 6*d* shows that the penetration of tracer is impeded by what appears to be a cell–cell junction between overlapping cellular processes. The tracer lines the cell membranes from the left, but

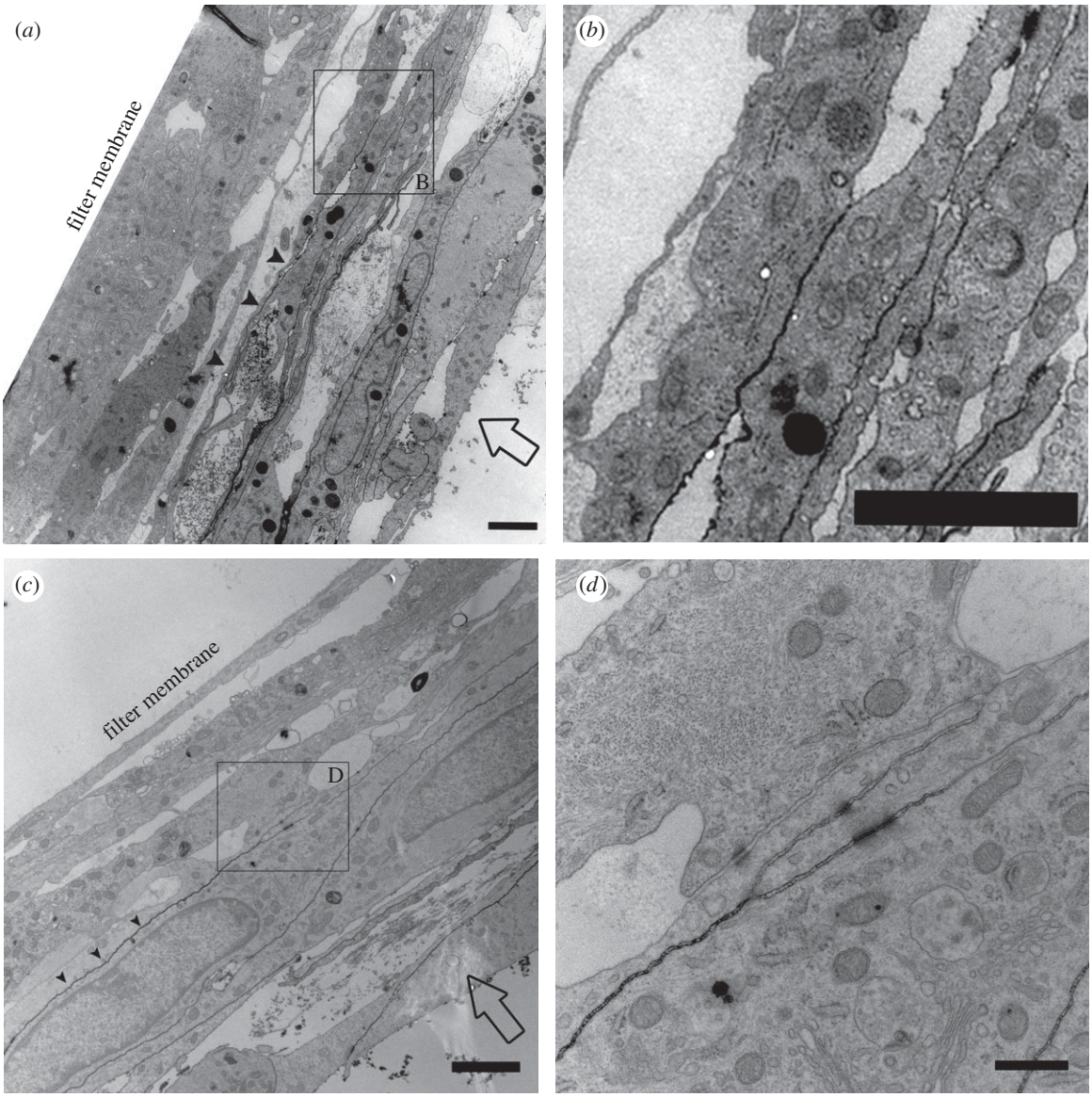

Figure 6. TEM analysis of ruthenium red tracer applied to apical cell membrane. AG cells were grown on inserts and not perfused (*a*,*b*) or fixed under 3 mm Hg A → B pressure (*c*,*d*). Ruthenium red (0.1%) was dissolved in the fixative and applied to the apical cell membrane (direction of flow indicated by open arrows, *a*,*c*). (*a*) Non-perfused control cells show ruthenium red tracer lining the cellular membranes (filled arrowheads) of the apical-most cell layers, but the tracer does not penetrate to the filter membrane. Scale bar, 2 μm. (*b*) Expanded view of an area from (*a*), showing where the tracer penetration is impeded presumably by cell–cell junction. Scale bar, 2 μm. (*c*) AG cells fixed under A → B pressure show similar penetration of the tracer (filled arrowheads) that is limited to the apical-most cell layers, but does not infiltrate the entire cell layer. Scale bar, 2 μm. (*d*) Magnified view of an area from (*c*) where the tracer penetration is impeded and accumulation of the tracer at a cell junction is visible. Scale bar, 0.5 μm.

begins to accumulate at the cell–cell junction and does not penetrate further to the right. It is apparent that the tracer does not infiltrate any further than this point as evidenced by the fact that the cell membranes closest to the filter membrane are not lined with tracer.

The electron micrographs for basolateral control cells (figure 7*a*,*b*) and cells perfused and fixed under B → A pressure (figure 7*c*,*d*) are qualitatively similar to those described above. Figure 7*d* (filled arrowheads) shows a magnified view of several overlapping cell layers close to the filter membrane where the tracer is visible accentuating cell membranes. Also visible is the point at which the tracer penetration is impeded (figure 6*d*, open arrowhead), likely by occluding cell–cell junctions that are not visible in the cross section shown here. Vacuoles without ruthenium red lining the inside may also be seen, indicating that these structures are totally contained within the cell (transcellular), rather than the pockets of the fluid that can be seen between cellular processes lined with ruthenium red (paracellular).

Taken together these micrographs indicate that the penetration of the ruthenium red tracer is similar regardless of whether or not the cells were perfused and fixed under pressure. Similarly, it appears that the tracer only penetrates several cell layers regardless of application of the tracer at the apical or basolateral aspect of the cell layer. It is also suggested that both paracellular and transcellular methods of fluid transport occur by studying the distribution of ruthenium red.

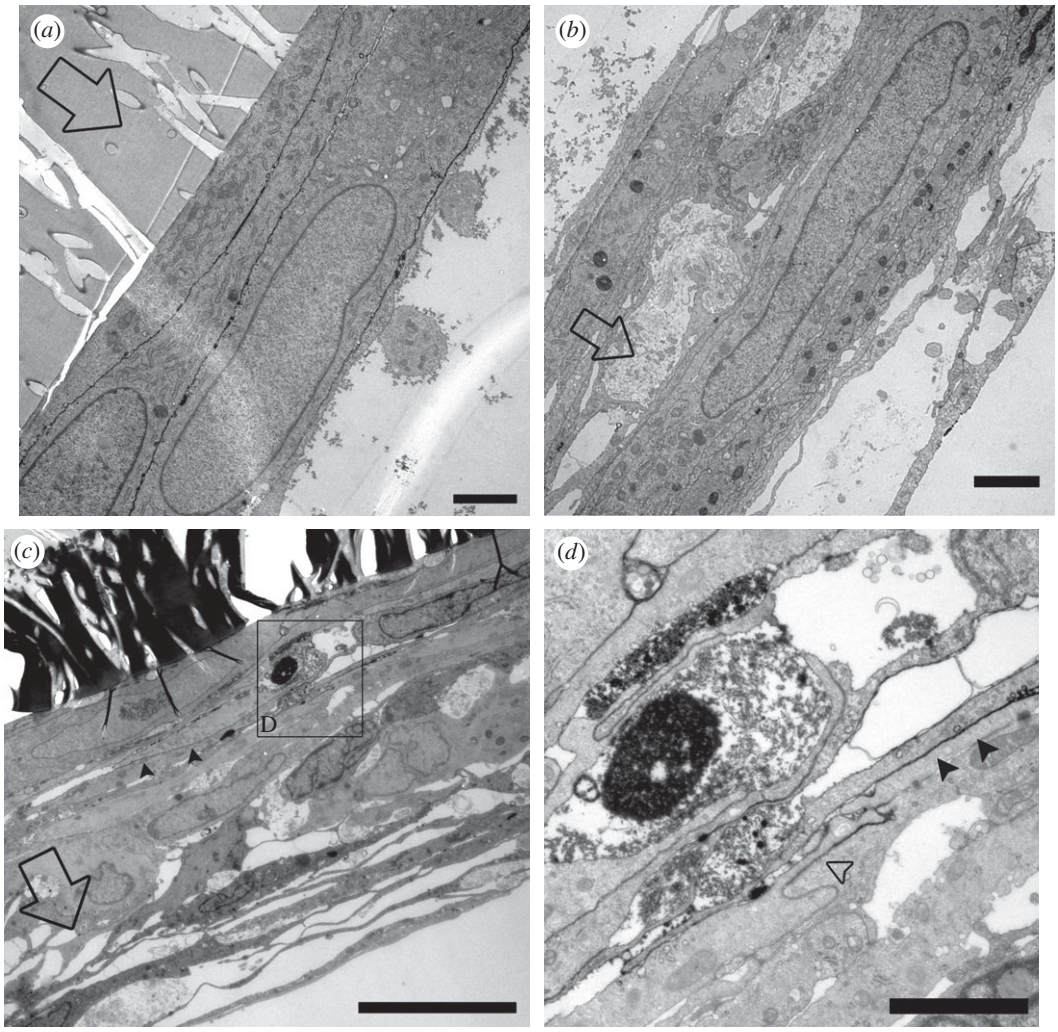

Figure 7. TEM of ruthenium red tracer applied to basolateral cell membranes. AG cells were grown on inserts and not perfused (*a*,*b*) or fixed under 3 mm Hg B → A pressure (*c*,*d*). Ruthenium red (0.1%) was dissolved in the fixative and applied to the apical cell membrane (open arrows indicate B → A direction of fixative movement, *a*–*c*). (*a*) Tracer penetration in non-perfused control cells was limited to the most basolateral cells immediately adjacent to the filter membrane. Scale bar, 2 μm. (*b*) The majority of the control cell layer became separated from the filter membrane during processing, but the tracer did not penetrate far enough to line these cells as evidenced by the lack of tracer lining cellular membranes (lower right corner of *b*). Scale bar, 2 μm. (*c*) AG cells fixed under B → A pressure show a similar depth of penetration of tracer as non-perfused control (filled arrowheads). Scale bar, 5 μm. (*d*) Expanded view from (*c*) showing that tracer penetration (filled arrowheads) is limited by the presence of cell–cell junctions (open arrowhead). Scale bar, 2 μm.

4. DISCUSSION

We have previously reported on the growth and characterization of cells cultured from human AG cells in serum. Using immunocytochemistry and flow cytometry, we demonstrated that it was possible to grow cells from human AG tissue consisting primarily of cells of arachnoidal origin (Holman *et al.* 2005). Furthermore, we have recently reported that these cells grown on permeable cell culture inserts display a directionality of fluid flow consistent with the circulation of CSF *in vivo* (Grzybowski *et al.* 2006).

In the present study, we have expanded on these initial experiments, taking into account the effect that the serum in the perfusion media has on the permeability characteristics of the culture inserts and AG cells. In addition, considering the limitations of EM, we have used a tracer molecule to help elucidate the path of fluid transport across these cells and to differentiate between inter- and intracellular structures.

The formation of tight junctions in AG cells was detected via immunocytochemical staining for ZO-1 and occludin proteins and was functionally assessed for cells grown on inserts using LY permeability. The LY permeability coefficient of AG cell layers grown on permeable filter inserts ranged from 11.04×10^{-6} cm s^{-1} on day 7 after seeding, and barrier integrity was found to maximize at 21 days post-seeding (P_{cell} of 7.19×10^{-6} cm s^{-1}). Together, these results suggest the presence of tight junctions; however, such junctions were not always readily apparent in the electron micrographs. Electron micrographs revealed the presence of numerous desmosomal junctions (figure 5*b*,*c*) as well as other areas of close membrane apposition (arrowheads in figure 5*b*), though it is not clear if these point contacts are in fact tight junctions. Cellular hydraulic conductivity of 17 human samples in serum-free conditions was shown to be 92.5 μl min^{-1} mm Hg^{-1} cm^{-2} with an average age of 60 years. A brief

pressure–flow study was performed using pressures ranging from physiological to supra-physiological (2–8 mm Hg) using SFM cells from two donors, four repetitions at each pressure. The resultant relationship was linear over the range. A second set of experiments using blank culture inserts with both SFM and media with 10 per cent serum showed that the culture inserts with SFM represented a negligible source of resistance when compared with the cellular layer. This linear relationship is consistent with numerous previous studies in both animals and humans (Welch & Pollay 1961; Ekstedt 1978; Czosnyka *et al.* 2004; Lenfeldt *et al.* 2007; Andersson *et al.* 2008). Further characterization of human permeability values under pathological conditions such as increased pressure and with increased loads of cytotoxic proteins is needed.

The presence of tight junction component protein, ZO-1, was shown using confocal microscopy and EM and was not affected by perfusion under pressure or removal of serum in the media. ZO-1 expression was maintained consistently around cell–cell borders, and suggests that during the perfusion in either direction AG cells maintain their tight junctions, and they may regulate the passage of fluid between cells (i.e. through the paracellular route). In addition, it is likely that these flow rates represent a true flow of fluid across the cell layer and are not an artefact of mechanical disruption of the cell layer owing to the imposed pressure.

4.1. Role of tight junctions in regulating CSF outflow

The role of cell–cell junctions between AG cells in regulating the outflow of CSF remains unclear. In addition to the transcellular vacuole pathway proposed by Tripathi (Tripathi 1973, 1974, 1977; Tripathi & Tripathi 1974), several authors have hypothesized that CSF is transported via paracellular routes as well (Shabo & Maxwell 1971; Gomez *et al.* 1973, 1974; Gomez & Potts 1977; Levine *et al.* 1982), presumably through widening of intercellular pathways. It has been shown that the perfusion pressure has an effect on the size of spaces between the cells lining the AGs in several species (Shabo & Maxwell 1971; Gomez *et al.* 1973, 1974; Gomez & Potts 1977; Levine *et al.* 1982). Since these cells form tight, occluding junctions, this may occur by the transient alteration in the 'tightness' of these junctions. It is well known that cells can regulate the tightness of occluding junctions through intracellular signalling mechanisms (Parisi 2001; Alvarado *et al.* 2004; Balda & Matter 2009). The potential role of this pathway in the outflow of CSF remains to be elucidated.

The 1 μm vacuolar structures visible in the EM images are similar to those structures previously described in intact AGs (Tripathi 1973, 1974, 1977; Tripathi & Tripathi 1974; Kida *et al.* 1988; Yamashima 1986, 1988), as well as the tissues of the eye involved in draining aqueous humour (Tripathi 1977; Grierson *et al.* 1979). The vacuolar mechanism of aqueous humour and CSF egress was first described by Tripathi (Tripathi 1968, 1973, 1974, 1977; Tripathi & Tripathi 1974) as a dynamic process involving the transient formation of large, transcellular vacuoles that transported fluid. These studies by Tripathi demonstrated that when contrast material was introduced into the cisterna magna or anterior chamber, the material was taken up by giant vacuoles found in the cells lining the AGs or the endothelium of Schlemm's canal within the eye, respectively (Tripathi 1968, 1977). The passage of tracer between intracellular clefts was prevented by tight cell–cell junctions in these tissues.

These studies focused primarily on the ultrastructural characteristics of vacuole formation, and have suggested that vacuoles may differ from other endocytic pathways most notably in the size of the vacuoles (of the order of several micrometres) compared with endocytic vesicles (of the order of 50–100 nm). In addition, the molecular components of these unique organelles remain unclear. At present, it is not known if large vacuolar structures share characteristics with other vesicular and endosomal transport processes, such as the expression of specific molecular markers of these pathways such as caveolin, clathrin or other SNARE proteins (Price *et al.* 1995; Doherty & McMahon 2009; Grant & Donaldson 2009). Additional experiments are warranted in order to identify specific vacuolar proteins that may be used as molecular tracers of large vacuole formation in AG cells.

To further study the path of fluid flow across cultured AG cells, the tracer ruthenium red was added to the fixative step in which cells were fixed under 3 mm Hg pressure. Ammoniated ruthenium oxychloride or ruthenium red ($H_{42}C_{l6}N_{14}O_2Ru_3$, molecular weight 786.36) is a cationic molecule that binds preferentially to the highly negatively charged glycosaminoglycans on the cell plasma membrane (Luft 1966, 1971*a*,*b*). Because it is highly charged, it is not taken up into the cell cytoplasm and can therefore be used to distinguish extracellular from intracellular structures. Additionally, similar to the tracer LY used to determine permeability coefficients, ruthenium red is a large charged molecule that in some cases can be used to delineate the presence of tight, occluding junctions.

Dispersion of ruthenium red through the AG cell layers was limited and did not fully penetrate the entire cell layer, regardless of whether the tracer was applied on the apical or basolateral side on the culture insert. It is possible that the diffusion of the tracer was impeded by the presence of tight junctions between overlapping and adjacent AG cells. In support of this explanation, AG cells perfused and fixed under pressure continue to express the tight junction protein ZO-1. Furthermore, the Z-stacked images showed ZO-1 expression at multiple depths through the cell layer (top and right panels in figure 4*b*,*c*), suggesting that the overlapping layers of AG cells on inserts form tight junctions. The expression of ZO-1 alone however is not sufficient to prove the formation of tight junctions. As previously mentioned, tight or occluding junctions were difficult to detect in the electron micrographs and it is possible that the penetration of the ruthenium tracer was limited owing to a diffusional barrier from the overlapping layers of AG cells.

As noted above, AG cells grew on inserts in multiple layers with processes of adjacent AG cells forming elongated overlapping zones. The extensive region of overlap between adjacent AG cells led to intercellular

clefts that formed tortuous channels. These clefts and interdigitating processes are reminiscent of structures described in some archaic fish species that form a glial blood–brain barrier (Bundgaard & Abbott 2008). In these species, extensively interdigitating perivascular glial processes surrounding blood vessels, rather than the presence of endothelial tight junctions, form a diffusion barrier to the tracer horseradish peroxidase, preventing it from reaching the brain parenchyma proper. In this study, Bundgaard & Abbott (2008) attempted to estimate the length of the diffusion pathway from the blood vessel endothelium through the overlapping glial processes to the parenchyma. In most cases, this was not possible because of the plane of the intercellular cleft leaving the plane of the EM section after 10–15 μm. In the limited instances where it was possible to estimate the diffusion path, the distance ranged from 10 to as much as 22 μm.

A similar estimate of the diffusion path length of the intercellular clefts between interdigitating AG cells should also be theoretically possible from the electron micrographs. Similar to the studies of the glial blood–brain barrier, in many cases it was not possible to examine the entire intercellular pathway from the apical to the basolateral edges. This was typically because of the plane of the AG cell layer leaving the plane or the edge of the electron micrograph. For example, when ruthenium red was applied at the apical edge of AG cells on inserts without pressure (figure 6*a*,*b*), the tracer penetrated through several layers of interdigitating cells but did fully diffuse to the filter membrane. The intercellular cleft where the tracer had diffused the deepest (figure 6*a*, just below the arrowheads) until the tracer stopped (inset B in figure 6*a*) was measured at approximately 25 μm. When the tracer was applied in the same apical direction while under pressure (figure 6*c*), the penetration of the tracer at its deepest point (figure 6*c*, below and left of arrowheads) until the penetration stops (figure 6*c*, inset D) measures at 10.5 μm. In experiments where ruthenium red was applied to the basolateral edge of the AG cell layer, the penetration depth of the tracer was comparable to the apical experiments. When the tracer was applied under pressure (figure 7*c*), the deepest penetration of the tracer (arrowheads in figure 7*c*, continuing up and right to inset) measured approximately 10 μm.

These measurements of the diffusion path of the ruthenium red tracer were made along the intercellular cleft where the tracer had most deeply penetrated the AG cell layer. In most cases, the actual length of the diffusion pathway was probably much greater because of the presence of multiple overlapping layers of cells. Regardless, the length of these pathways was comparable when the tracer was applied at the apical or basolateral edge of the cell layer. Together, these results suggest that elongated overlapping layers of AG cells may also provide an additional diffusional barrier that could potentially regulate the passage of fluid or macromolecules across the AGs.

4.2. *Comparison of* in vitro *and computational model results*

The computational model presented in part I of this study was based on *in vivo* MRI data to calculate the transient, three-dimensional CSF flow field in a human subarachnoid space (Gupta *et al.* 2010). This model predicts the hydraulic conductivity of the arachnoid granulations to be 130.9 $\mu l\,min^{-1}\,mm\,Hg^{-1}\,cm^{-2}$, which is about 40 per cent higher than the experimentally observed *in vitro* hydraulic conductivity of 92.5 $\mu l\,min^{-1}\,mm\,Hg^{-1}\,cm^{-2}$. Remarkably, these numbers are extremely close to the predicted 60 per cent CSF outflow through the AGs at physiological pressures using animal models, with the remaining 40 per cent assumed to be exiting the cranial space through lymphatics (Boulton *et al.* 1998*a*). This is, to our knowledge, the first time that an estimate of CSF outflow from the subarachnoid space in humans has been presented either experimentally or computationally.

There are a number of assumptions made that may contribute to the difference in hydraulic conductivity values between the two models. One of these is that the computational model calculates L_p via the net CSF flow, which should correspond to the production/absorption rate of CSF. However, absorption sites other than the AGs are neglected, which means that for a given pressure difference, the L_p has to be higher to compensate for the lack of other absorption pathways.

Lymphatic drainage driven by filtration pressure, contraction of adjacent muscles and pulsations of neighbouring arteries (Schley *et al.* 2006; Gupta *et al.* 2009) predicts the subarachnoid space to be compliant, but with minimal deformation throughout the cardiac cycle, which would translate to a lymphatic component that is less than that previously predicted using animals (Boulton *et al.* 1998*b*).

In addition, the computational model uses only a rough estimate for the active area of the AGs, which calculates a proportional AG to total en face surface area using 35 formalin-fixed human brains. This number is an estimate based on a relatively small subject population and needs to be studied further.

Other areas that might contribute to differences between the computational and *in vitro* model are the difficulties encountered in obtaining the net CSF flow via MRI. The variation of values presented in the literature is enormous. Based on the inherent variability, using the most currently available technologies still generates errors of approximately ± 10–20%.

The *in vitro* model does not presently consider pulsatility as a variable, but doing so in the future would generate results closer to physiological direction. Pulsatility has been shown to affect cardiovascular endothelial permeability in various models (Hazel *et al.* 2003; Alberding *et al.* 2004; Himburg 2004) and is expected to affect CSF outflow through the mesothelial arachnoidal cells.

Another very important difference between the *in vitro* and computational models is the difference in age of the human subjects. The average age of tissue donors for the *in vitro* model was 60, while the age of the subject for the computational model was in the 20's. It has been shown that both production and egress of CSF decrease with age and in pathological conditions, such as Alzheimer's disease (Selkoe 2000;

Silverberg *et al.* 2001, 2003), a higher L_p would be expected from a human subject in their 20's when compared with one in their 60's, as was used in the *in vitro* model experimental L_p values.

We present a functional and structural pathology of the AM absorptive mechanism which furthers our understanding of the important role AM plays in the clearance of CSF and toxic metabolites. Using cultures of human AG cells and a specialized perfusion system, we have shown that this model mimics *in vivo* characteristics of unidirectional fluid transport, maintenance of tight junctions and permeability values that are in agreement with the CSF outflow rates derived from the results of a dynamic computational model of the subarachnoid cranial space.

Together, the combination of the computational model with the human *in vitro* model creates the first reported system capable of studying CSF dynamics functionally and structurally in health and in disease. Using both *in vitro* and computational approaches will permit the study of CSF retention or stagnation, with the formation of a 'ventricular sink' of metabolic products of neurodegeneration, and their role as neurotoxins in the cascade of events leading to the signs and symptoms of diseases such as Alzheimer's disease, and to their progression (Stopa 2001; Kivisakk 2003; Silverberg *et al.* 2003).

We would like to thank the Ohio Lions Eye Research Facility and the North American NeuroOphthalmology Society for financial support of this work. We would like to thank the Swiss National Science Foundation for support of this work through SmartShunt—The Hydrocephalus Project. This work was partially funded by the Ohio Lions Eye Research Foundation. D.W.H. designed and executed the experiments, performed sample analysis and statistical analysis and also assisted with manuscript preparation. V.K. conceived, designed and directed all computational model work and assisted with manuscript preparation. D.M.G. conceived, designed and directed all *in vitro* model work and assisted with manuscript preparation. In addition, we would like to thank Jeff Pelley and the staff at the OSU Autopsy Center for their assistance in procuring tissue samples, and Kathy Wolken and Brian Kemmenoe of the Campus Microscopy and Imaging Facility for their assistance with all of the imaging and sample preparation for this work.

REFERENCES

Abbott, N. J. 2005 Dynamics of CNS barriers: evolution, differentiation, and modulation. *Cell. Mol. Neurobiol.* **25**, 5–23. (doi:10.1007/s10571-004-1374-y)

Alberding, J. P., Baldwin, A. L., Barton, J. K. & Wiley, E. 2004 Onset of pulsatile pressure causes transiently increased filtration through artery wall. *Am. J. Physiol. Heart Circ. Physiol.* **286**, H1827–H1835. (doi:10.1152/ajpheart.01059.2003)

Alvarado, J. A., Betanzos, A., Franse-Carman, L., Chen, J. & Gonzalez-Mariscal, L. 2004 Endothelia of Schlemm's canal and trabecular meshwork: distinct molecular, functional, and anatomic features. *Am. J. Physiol. Cell Physiol.* **286**, C621–C634. (doi:10.1152/ajpcell.00108.2003)

Andersson, N., Malm, J. & Eklund, A. 2008 Dependency of cerebrospinal fluid outflow resistance on intracranial pressure. *J. Neurosurg.* **109**, 918–922. (doi:10.3171/JNS/2008/109/11/0918)

Balda, M. S. & Matter, K. 2009 Tight junctions and the regulation of gene expression. *Biochim. Biophys. Acta* **1788**, 761–767. (doi:10.1016/j.bbamem.2008.11.024)

Boulton, M., Armstrong, D., Flessner, M., Hay, J., Szalai, J. P. & Johnston, M. 1998*a* Raised intracranial pressure increases CSF drainage through arachnoid villi and extracranial lymphatics. *Am. J. Physiol.* **275**, R889–R896.

Boulton, M., Flessner, M., Armstrong, D., Hay, J. & Johnston, M. 1998*b* Determination of volumetric cerebrospinal fluid absorption into extracranial lymphatics in sheep. *Am. J. Physiol.* **274**, R88–R96.

Bundgaard, M. & Abbott, N. J. 2008 All vertebrates started out with a glial blood-brain barrier 4–500 million years ago. *Glia* **56**, 699–708. (doi:10.1002/glia.20642)

Czosnyka, M., Czosnyka, Z., Momjian, S. & Pickard, J. D. 2004 Cerebrospinal fluid dynamics. *Physiol. Meas.* **25**, R51–R76. (doi:10.1088/0967-3334/25/5/R01)

Deli, M. A., Abraham, C. S., Kataoka, Y. & Niwa, M. 2005 Permeability studies on *in vitro* blood–brain barrier models: physiology, pathology, and pharmacology. *Cell. Mol. Neurobiol.* **25**, 59–127. (doi:10.1007/s10571-004-1377-8)

Doherty, G. J. & McMahon, H. T. 2009 Mechanisms of endocytosis. *Annu. Rev. Biochem.* **78**, 857–902. (doi:10.1146/annurev.biochem.78.081307.110540)

Ekstedt, J. 1978 CSF hydrodynamic studies in man. 2. Normal hydrodynamic variables related to CSF pressure and flow. *J. Neurol. Neurosurg. Psychiatry* **41**, 345–353. (doi:10.1136/jnnp.41.4.345)

Gomez, D. G. & Potts, D. G. 1977 Effects of pressure on the arachnoid villus. *Exp. Eye Res.* **25**(Suppl.), 117–125. (doi:10.1016/S0014-4835(77)80011-0)

Gomez, D. G., Potts, G., Deonarine, V. & Reilly, K. F. 1973 Effects of pressure gradient changes on the morphology of arachnoid villi and granulations of the monkey. *Lab. Invest.* **28**, 648–657.

Gomez, D. G., Potts, D. G. & Deonarine, V. 1974 Arachnoid granulations of the sheep. Structural and ultrastructural changes with varying pressure differences. *Arch. Neurol.* **30**, 169–175.

Grant, B. D. & Donaldson, J. G. 2009 Pathways and mechanisms of endocytic recycling. *Nat. Rev. Mol. Cell Biol.* **10**, 597–608. (doi:10.1038/nrm2755)

Grierson, I., Lee, W. R., Moseley, H. & Abraham, S. 1979 The trabecular wall of Schlemm's canal: a study of the effects of pilocarpine by scanning electron microscopy. *Br. J. Ophthalmol.* **63**, 9–16. (doi:10.1136/bjo.63.1.9)

Grzybowski, D. M., Holman, D. W., Katz, S. E. & Lubow, M. 2006 *In vitro* model of cerebrospinal fluid outflow through human arachnoid granulations. *Invest. Ophthalmol. Vis. Sci.* **47**, 3664–3672. (doi:10.1167/iovs.05-0929)

Gupta, S., Soellinger, M., Boesiger, P., Poulikakos, D. & Kurtcuoglu, V. 2009 Three-dimensional computational modeling of subject-specific cerebrospinal fluid flow in the subarachnoid space. *J. Biomech. Eng.* **131**, 021010. (doi:10.1115/1.3005171)

Gupta, S. *et al.* 2010 Cerebrospinal fluid dynamics in the human cranial subarachnoid space: an overlooked mediator of cerebral disease. I. Computational model. *J. R. Soc. Interface.* **7**, 1195–1204. (doi:10.1098/rsif.2010.0033)

Hazel, A. L., Grzybowski, D. M. & Friedman, M. H. 2003 Modeling the adaptive permeability response of porcine iliac arteries to acute changes in mural shear. *Ann. Biomed. Eng.* **31**, 412–419. (doi:10.1114/1.1560633)

Himburg, H. A., Grzybowski, D. M., Hazel, A. L., LaMack, J. A., Li, X.-M. & Friedman, M. H. 2004 Spatial comparison between wall shear stress measures and porcine arterial endothelial permeability. *Am. J. Physiol. Heart Circ.*

Physiol. **286**, H1916–H1922. (doi:10.1152/ajpheart.00897.2003)

Holman, D. W., Grzybowski, D. M., Mehta, B. C., Katz, S. E. & Lubow, M. 2005 Characterization of cytoskeletal and junctional proteins expressed by cells cultured from human arachnoid granulation tissue. *Cerebrospinal Fluid Res.* **2**, 9. (doi:10.1186/1743-8454-2-9)

Johanson, C., Del Bigio, M., Kinsman, S., Miyan, J., Pattisapu, J., Robinson, M. & Jones, H. C. 2001 New models for analysing hydrocephalus and disorders of CSF volume transmission. *Br. J. Neurosurg.* **15**, 281–283. (doi:10.1080/026886901750353782)

Johanson, C., McMillan, P., Tavares, R., Spangenberger, A., Duncan, J., Silverberg, G. & Stopa, E. 2004 Homeostatic capabilities of the choroid plexus epithelium in Alzheimer's disease. *Cerebrospinal Fluid Res.* **1**, 3. (doi:10.1186/1743-8454-1-3)

Johanson, C. E., Duncan, J. A., Stopa, E. G. & Baird, A. 2005 Enhanced prospects for drug delivery and brain targeting by the choroid plexus-CSF route. *Pharm. Res.* **22**, 1011–1037. (doi:10.1007/s11095-005-6039-0)

Johnston, I. & Teo, C. 2000 Disorders of CSF hydrodynamics. *Child's Nerv. Syst.* **16**, 776–799. (doi:10.1007/s003810000383)

Johnston, I., Hawke, S., Halmagyi, M. & Teo, C. 1991 The pseudotumor syndrome. Disorders of cerebrospinal fluid circulation causing intracranial hypertension without ventriculomegaly. *Arch. Neurol.* **48**, 740–747.

Jones, H. C. 1985 Cerebrospinal fluid pressure and resistance to absorption during development in normal and hydrocephalic mutant mice. *Exp. Neurol.* **90**, 162–172. (doi:10.1016/0014-4886(85)90049-4)

Kida, S., Yamashima, T., Kubota, T., Ito, H. & Yamamoto, S. 1988 A light and electron microscopic and immunohistochemical study of human arachnoid villi. *J. Neurosurg.* **69**, 429–435. (doi:10.3171/jns.1988.69.3.0429)

Kivisakk, P. *et al.* 2003 Human cerebrospinal fluid central memory CD4+ T cells: evidence for trafficking through choroid plexus and meninges via P-selectin. *Proc. Natl Acad. Sci. USA* **100**, 8389–8394. (doi:10.1073/pnas.1433000100)

Lenfeldt, N., Koskinen, L. O., Bergenheim, A. T., Malm, J. & Eklund, A. 2007 CSF pressure assessed by lumbar puncture agrees with intracranial pressure. *Neurology* **68**, 155–158. (doi:10.1212/01.wnl.0000250270.54587.71)

Levine, D. N. 2000 Ventricular size in pseudotumor cerebri and the theory of impaired CSF absorption. *J. Neurol. Sci.* **177**, 85–94. (doi:10.1016/S0022-510X(00)00348-8)

Levine, J. E., Povlishock, J. T. & Becker, D. P. 1982 The morphological correlates of primate cerebrospinal fluid absorption. *Brain Res.* **241**, 31–41. (doi:10.1016/0006-8993(82)91225-2)

Luft, J. H. 1966 Fine structures of capillary and endocapillary layer as revealed by ruthenium red. *Fed. Proc.* **25**, 1773–1783.

Luft, J. H. 1971*a* Ruthenium red and violet. II. Fine structural localization in animal tissues. *Anat. Rec.* **171**, 369–415. (doi:10.1002/ar.1091710303)

Luft, J. H. 1971*b* Ruthenium red and violet. I. Chemistry, purification, methods of use for electron microscopy and mechanism of action. *Anat. Rec.* **171**, 347–368. (doi:10.1002/ar.1091710302)

Martins, A. N., Ramirez, A., Solomon, L. S. & Wiese, G. M. 1974 The effect of dexamethasone on the rate of formation of cerebrospinal fluid in the monkey. *J. Neurosurg.* **41**, 550–554. (doi:10.3171/jns.1974.41.5.0550)

Parisi, V., Restuccia, R., Fattapposta, F., Mina, C., Bucci, M. G. & Pierelli, F. 2001 Morphological and functional retinal impairment in Alzheimer's disease patients. *Clin. Neurophysiol.* **112**, 1860–1867. (doi:10.1016/S1388-2457(01)00620-4)

Price, D. A., Clayton, P. E. & Lloyd, I. C. 1995 Benign intracranial hypertension induced by growth hormone treatment. *Lancet* **345**, 458–459. (doi:10.1016/S0140-6736(95)90444-1)

Schley, D., Carare-Nnadi, R., Please, C. P., Perry, V. H. & Weller, R. O. 2006 Mechanisms to explain the reverse perivascular transport of solutes out of the brain. *J. Theor. Biol.* **238**, 962–974. (doi:10.1016/j.jtbi.2005.07.005)

Segal, M. B. 2000 The choroid plexuses and the barriers between the blood and the cerebrospinal fluid. *Cell. Mol. Neurobiol.* **20**, 183–196. (doi:10.1023/A:1007045605751)

Selkoe, D. J. 2000 Toward a comprehensive theory for Alzheimer's disease. Hypothesis: Alzheimer's disease is caused by the cerebral accumulation and cytotoxicity of amyloid β-protein. *Ann. NY Acad. Sci.* **924**, 17–25.

Shabo, A. L. & Maxwell, D. S. 1971 The fine structure of the primate arachnoid villus under normal and experimental conditions. *Acta Neurol. Latinoam.* **1**(Suppl. 1), 53–87.

Silverberg, G. D., Heit, G., Huhn, S., Jaffe, R. A., Chang, S. D., Bronte-Stewart, H., Rubenstein, E., Possin, K. & Saul, T. A. 2001 The cerebrospinal fluid production rate is reduced in dementia of the Alzheimer's type. *Neurology* **57**, 1763–1766.

Silverberg, G. D., Mayo, M., Saul, T., Rubenstein, E. & McGuire, D. 2003 Alzheimer's disease, normal-pressure hydrocephalus, and senescent changes in CSF circulatory physiology: a hypothesis. *Lancet Neurol.* **2**, 506. (doi:10.1016/S1474-4422(03)00487-3)

Stopa, E. G., Berzin, T. M., Kim, S., Song, P., Kuo-LeBlanc, V., Rodriguez-Wolf, M., Baird, A. & Johanson, C. E. 2001 Human choroid plexus growth factors: what are the implications for CSF dynamics in Alzheimer's disease? *Exp. Neurol.* **167**, 40–47. (doi:10.1006/exnr.2000.7545)

Tripathi, R. C. 1968 Ultrastructure of Schlemm's canal in relation to aqueous outflow. *Exp. Eye Res.* **7**, 335–341. (doi:10.1016/S0014-4835(68)80047-8)

Tripathi, R. C. 1973 Ultrastructure of the arachnoid mater in relation to outflow of cerebrospinal fluid. A new concept. *Lancet* **2**, 8–11. (doi:10.1016/S0140-6736(73)91945-4)

Tripathi, R. 1974 Tracing the bulk outflow route of cerebrospinal fluid by transmission and scanning electron microscopy. *Brain Res.* **80**, 503–506. (doi:10.1016/0006-8993(74)91033-6)

Tripathi, R. C. 1977 The functional morphology of the outflow systems of ocular and cerebrospinal fluids. *Exp. Eye Res.* **25**, 65–116. (doi:10.1016/S0014-4835(77)80010-9)

Tripathi, B. J. & Tripathi, R. C. 1974 Vacuolar transcellular channels as a drainage pathway for cerebrospinal fluid. *J. Physiol.* **239**, 195–206.

Welch, K. & Pollay, M. 1961 Perfusion of particles through arachnoid villi of the monkey. *Am. J. Physiol.* **201**, 651–654.

Yamashima, T. 1986 Ultrastructural study of the final cerebrospinal fluid pathway in human arachnoid villi. *Brain Res.* **384**, 68–76. (doi:10.1016/0006-8993(86)91220-5)

Yamashima, T. 1988 Functional ultrastructure of cerebrospinal fluid drainage channels in human arachnoid villi. *Neurosurgery* **22**, 633–641. (doi:10.1097/00006123-198804000-00003)